INTERNATIONAL JOURNAL FOR NUMERICAL METHODS IN FLUIDS, VOL. 17, 1055–1077 (1993)

NUMERICAL SIMULATION OF THE HEAD-ON REFLECTION OF A REGULAR REFLECTION

J. FALCOVITZ

Faculty of Aerospace Engineering, Technion – Israel Institute of Technology, Haifa, Israel

G. ALFANDARY

Rafael Ballistics Center, P.O. Box 2250, Haifa, Israel

AND

G. BEN-DOR

Pearlstone Center for Aeronautical Engineering Studies, Department of Mechanical Engineering,
Ben-Gurion University of the Negev, Beer Sheva, Israel

SUMMARY

The head-on collision and subsequent reflection of a Regular Reflection (RR) from the end-wall of a shock tube has been investigated both experimentally and numerically for two different incident shock wave Mach numbers and two different reflecting wedge angles.

The agreement between the double-exposure holographic interferograms and the numerical simulations which were obtained using a GRP based numerical code, was found to be excellent in the RR region and very good behind the head-on reflected RR.

The overall good agreement between the computed and experimental constant-density contours (isopycnics) constitutes a validation of the computational method, including the oblique-wall boundary condition.

KEY WORDS Computational fluid dynamics, Shock wave reflections, Regular reflection

INTRODUCTION

When a planar shock wave collides with an oblique planar surface, it reflects over it either as a Regular Reflection (RR) or as an Irregular Reflection (IR) depending upon the incident shock wave Mach number, M_i, and the reflecting wedge angle, θ_w.

A schematic illustration of the wave configuration of a regular reflection, which is the subject of the present study, is shown in Figure 1. As can be seen, the regular reflection consists of two discontinuities, namely, the incident shock wave, i, and the reflected shock wave, r, which meet on the reflecting wedge surface at the reflection point, R. The corner-generated signals (shown in Figure 1 by a dashed line) divide the reflected shock wave, r, at point c into two parts: a curved part and a straight part. Since the flow states (0), (1) and (2) are bounded by straight discontinuities, they are uniform provided the gas is assumed to be a perfect fluid (i.e. $\mu=0$, and $k=0$, where μ is the dynamic viscosity and k is the thermal conductivity). In a frame of reference attached to the reflection point R, the flow in states (0), (1) and (2) is supersonic, i.e. $M_0^R>1$, $M_1^R>1$ and $M_2^R>1$, where M_i^R is the flow Mach number in state (i) with respect to point R. Note that $M_2^R>1$

0271–2091/93/241055–23$16.50

Received January 1993
Revised August 1993

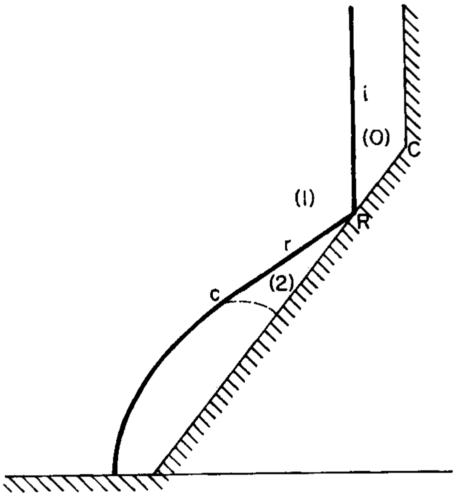

Figure 1. Schematic illustration of the wave configuration of a regular reflection—RR

is the condition for the existence of a regular reflection, since the RR↔IR transition occurs at $M_2^R = 1$. For more details, the interested reader is referred to Ben-Dor.[1]

When the reflection point, R, reaches the corner C at the end of the reflecting wedge, the incident shock wave reflects head-on and interacts with the reflected shock wave, r. The interaction of the head-on and the regularly reflected shock waves result in the wave configuration shown in Figure 2. The wave configuration consists basically of two triple points, T_1 and T_2, which have a common Mach stem, m_{12}, which, in general, is not straight but slightly curved. Note that this reflection process is a particular case of the more general reflection process which was recently investigated analytically and experimentally by Ben-Dor *et al.*[2] and numerically by Itoh *et al.*[3]

The resulting wave configuration grows linearly from the corner C, i.e. it is self-similar, as long as the second triple point, T_2, has not reached point c, which as mentioned earlier is the point reached by the corner-generated signals along the regularly reflected shock wave, r.

The aim of the present study is to develop a numerical code which can capture the above-mentioned reflection process with high resolution and to conduct a reliability test of the numerical method by comparing its results with actual shock tube experiments visualized using double-exposure holographic interferometry. The present numerical code is based on the Generalized Riemann Problem (GRP) scheme for compressible flows. It was applied to simulate the head-on reflection process of a regular reflection from the end-wall of the shock tube for the conditions given in Table I.

EXPERIMENTS

The experiments were conducted using a 60 mm × 150 mm shock tube of the Shock Wave Research Center of the Institute of Fluid Science of Tohoku University. The driver section was 1·5 m long and had a diameter of 230 mm. The driver gas was air at room temperature (290–293 K). The length of the driven section (the channel) was 8 m. The test section windows were made of BK7. Their dimensions were 150 mm × 230 mm. The test gas was dry air at room

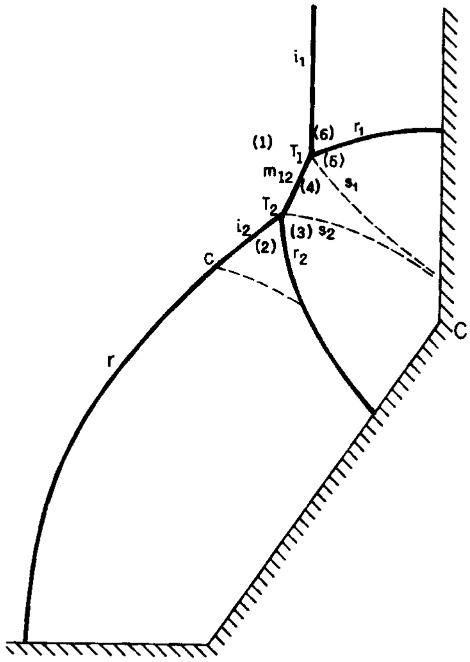

Figure 2. Schematic illustration of the wave configuration which results following the head-on reflection of the regular reflection at the shock tube end-wall

Table I. Conditions of the three investigated cases (a)

Case No.	M_i[b]	θ_w	Grid
1	1·26	55°	220 × 190[c]
2	1·48	55°	235 × 175[c] 705 × 525[d]
3	1·26	65°	660 × 480[d]

[a] The experiments were conducted in dry air at $P_0 \approx 760$ mmHg and $T_0 \approx 290$–293 K

[b] This is an average value out of three to five experiments

[c] Coarse mesh. Square cells

[d] Fine mesh. Square cells

temperature (290–293 K) and atmospheric pressure (~760 mmHg). The incident shock wave velocity was recorded using Kistler pressure transducers which were flash mounted in the upper wall of the shock tube just ahead of the test section. The attenuation of the incident shock wave was checked and found to be negligibly small.

Double-exposure holographic interferometry was used to record the investigated interaction. The light source was a Q-switched giant-pulse ruby laser ($\lambda = 694{\cdot}3$ nm) having a pulse width of 20 ns and an energy of about 1 J per pulse.

NUMERICAL METHOD

The two-dimensional plane-symmetric flow phenomenon under consideration here was computed by a 2D code based on the GRP scheme for compressible inviscid flows.[4] (Note, however, that in Reference 4 a duct flow is treated; here the scheme is reduced to plane symmetry by assuming unit duct area throughout.) The 1D GRP scheme was extended to the present 2D code by employing a second-order-preserving operator splitting fashioned after Strang,[5] augmented by an oblique wall boundary condition. In the following, an outline of the GRP scheme along with the 2D extension features are presented.

The GRP scheme is best described as combining the exactness of a formulation based on compatibility relations along characteristic lines in (x, t), with the robustness and shock capturing features of a conservation laws scheme. The discretization scheme is a piecewise linear approximation of flow variables per cell, with discontinuities at cell interfaces. The key idea is to evaluate the fluxes of mass, momentum and energy from exact solutions to the GRPs that arise at each cell interface; in particular, these fluxes are second-order accurate in time, since each flux component and its time derivative are determined analytically. The fluxes are subsequently incorporated in a discrete time integration scheme for the average densities of mass, momentum and energy per cell, resulting in second-order accurate integration of the hydrodynamic conservation laws.

Consider the Euler equations governing the time-dependent flow of an inviscid compressible fluid in (x, t):

$$\frac{\partial}{\partial t}\mathbf{U}+\frac{\partial}{\partial x}\mathbf{F}(\mathbf{U})=0 \tag{1a}$$

$$\mathbf{U}(x,t)=\begin{bmatrix}\rho\\ \rho u\\ \rho E\end{bmatrix},\qquad \mathbf{F}(\mathbf{U})=\begin{bmatrix}\rho u\\ \rho u^2+p\\ (\rho E+p)u\end{bmatrix}, \tag{1b}$$

$$E=e+\tfrac{1}{2}u^2,\qquad p=(\gamma-1)\rho e, \tag{1c}$$

where ρ, p, e, u and γ are the density, pressure, specific energy, velocity and specific heat capacities ratio (in the present study a perfect gas is assumed). The grid comprises equally spaced cell-interface points $x_{i+1/2}=(i+1/2)\Delta x$, where Δx is the grid spacing and cell i is the interval $x_{i-1/2}<x<x_{i+1/2}$ centred about the point $x_i=i\Delta x$. The conservative second-order difference scheme for the time integration of the hydrodynamic conservation laws is

$$\begin{aligned}&\mathbf{U}_i^{n+1}=\mathbf{U}_i^n-\frac{\Delta t}{\Delta x}\left[\mathbf{F}(\mathbf{U})_{i+1/2}^{n+1/2}-\mathbf{F}(\mathbf{U})_{i-1/2}^{n+1/2}\right],\\ &\Delta t=t^{n+1}-t^n,\end{aligned} \tag{2}$$

where the time-centred fluxes $\mathbf{F}(\mathbf{U})_{i+1/2}^{n+1/2}$ are obtained by the following procedure.[4] The flow at time level t^n is approximated as piecewise linear in cells (Figure 3). The Riemann problems that correspond to the initial discontinuity $[\mathbf{U}_\mathrm{L}, \mathbf{U}_\mathrm{R}]$ at cell interfaces are solved, giving rise to the first-order (upwinded) fluxes $\mathbf{F}(\mathbf{U})_{i+1/2}^n$. This is followed by the evaluation of the first time-derivative of flow variables at cell interfaces $\partial/\partial t\,((\mathbf{U})_{i+1/2}^n)$, using analytic expressions that resulted from the GRP analysis. The stage is then set for evaluating the second-order accurate

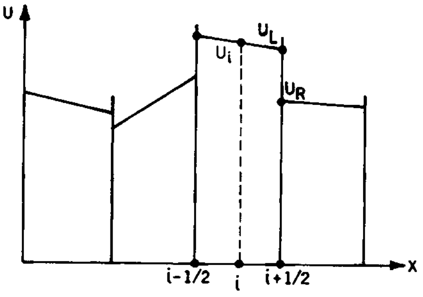

Figure 3. The GRP spatial discretization scheme

fluxes given by

$$\mathbf{F}(\mathbf{U})^{n+1/2}_{i+1/2}=\mathbf{F}(\mathbf{U}^n_{i+1/2})+\frac{\Delta t}{2}\left[\frac{\partial}{\partial t}\mathbf{F}(\mathbf{U})\right]^n_{i+1/2}+O(\Delta t^2),$$
$$\left[\frac{\partial}{\partial t}\mathbf{F}(\mathbf{U})\right]^n_{i+1/2}=\mathbf{F}'(U^n_{i+1/2})\left[\frac{\partial}{\partial t}\mathbf{U}\right]^n_{i+1/2}, \tag{3}$$

where the notation $\mathbf{F}'(\mathbf{U})$ denotes the Jacobian matrix of $\mathbf{F}$, with respect to $\mathbf{U}$.

Following the integration of the conservation laws, the 1D scheme requires an updating of the slopes of the flow variables in the cells, subjected to monotonicity constraints designed to avoid erroneous interpolations through hydrodynamic jumps (shocks, contacts); the Van-Leer[6] monotonicity scheme was imposed on the slopes of primitive variables (u, ρ, p and v in the 2D case).

Turning to the case of flow in two space dimensions, the 2D Euler equations in (x, y, t) are as follows:

$$\frac{\partial}{\partial t}\mathbf{U}+\frac{\partial}{\partial x}\mathbf{F}(\mathbf{U})+\frac{\partial}{\partial y}\mathbf{G}(\mathbf{U})=0, \tag{4a}$$

$$\mathbf{U}(x,y,t)=\begin{bmatrix}\rho\\ \rho u\\ \rho v\\ \rho E\end{bmatrix},\quad \mathbf{F}(\mathbf{U})=\begin{bmatrix}\rho u\\ \rho u^2+p\\ \rho uv\\ (\rho E+p)u\end{bmatrix},\quad \mathbf{G}(\mathbf{U})=\begin{bmatrix}\rho v\\ \rho uv\\ \rho v^2+p\\ (\rho E+p)v\end{bmatrix}, \tag{4b}$$

$$E=e+\tfrac{1}{2}(u^2+v^2),\qquad p=(\gamma-1)\rho e, \tag{4c}$$

where u, v are the velocity components, and $\mathbf{F}(\mathbf{U}), \mathbf{G}(\mathbf{U})$ are the flux components in the x, y directions, respectively. An operator-splitting is now performed on equation (4), whereby the 2D equations are split into a set of two 1D equations, each of which is identical to equation (1) except for the addition of a fourth equation expressing the conservation of the transverse-momentum component. The splitting is represented by the 1D operators, L_x, L_y as follows:

$$L_x \text{ by } \frac{\partial}{\partial t}\mathbf{U}+\frac{\partial}{\partial x}\mathbf{F}(\mathbf{U})=0,$$
$$L_y \text{ by } \frac{\partial}{\partial t}\mathbf{U}+\frac{\partial}{\partial y}\mathbf{G}(\mathbf{U})=0. \tag{5}$$

Generally speaking, a finite difference integration of L_x followed by a similar integration of L_y constitutes a split finite difference integration of the 2D conservation laws given by equation (4). We actually employed this very simple splitting scheme denoted as L_xL_y in the computations presented subsequently. The reasoning behind this choice is the following. In an analysis of operator splitting by Strang,[5] it was shown that the combination of fractional split operators $L_x^{1/2}L_y^1L_x^{1/2}$, where the superscripts denote a fraction of the integration time-step, constituted a second-order accurate integration of the 2D equations, provided each split operator was second-order accurate by itself. Since we are seeking to obtain a numerical solution through a sequence of many time steps, we argue that by lumping the closing half-step $L_x^{1/2}$ of a previous time cycle with the opening one of the following cycle, an error of $O(\Delta t^2)$ is committed, which is consistent with the overall second-order accuracy of the scheme. The resulting split scheme is the simplest one, namely, $L_x^1L_y^1$.

Our operator splitting scheme is elucidated by considering the intuitive two-stage advection illustrated in Figure 4. The $L_x^1L_y^1$ combination gives rise to a displacement of a lump of fluid through a grid corner (Figure 4) having a volume $uv\Delta t^2$, i.e. of second-order magnitude. This feature of the splitting scheme results from the consecutive application of $L_x^1L_y^1$; it would not have been obtained had the two operators been performed simultaneously.

The only modifications to the truly 1D GRP scheme are the inclusion of the transverse velocity components in the expression for kinetic energy, and the addition of a transverse momentum conservation law. It is sufficient to consider the L_x operator, since the L_y operator can be derived by analogy. The flux of ρuv is treated by the GRP scheme as a pure advection since the accelerating y-component of the pressure gradient is absent from L_x. Physically speaking, this corresponds to the assumption that fluid particles advected through cell interfaces retain their

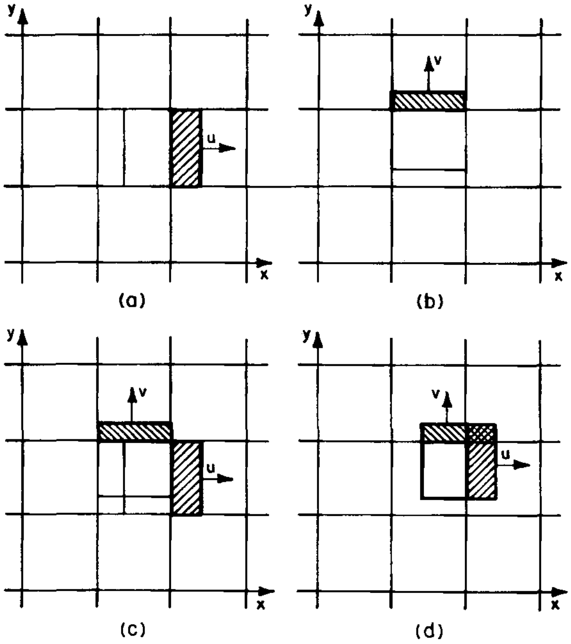

Figure 4. Illustration of the operator splitting scheme as uniform advection: (a) single L_x^1 integration; (b) single L_y^1 integration; (c) simultaneous $L_x^1L_y^1$ integration; (d) split $L_x^1L_y^1$ integration

transverse velocity component v throughout the time-step Δt, regardless of any wave structure resolving the discontinuity at t^n at each cell interface. However, since the average gradient $\partial v/\partial\xi$ per cell is to be accounted for (ξ is the local Lagrange co-ordinate defined as $d\xi=\rho dx$), the flux ρuv at $i+1/2$ is not constant throughout the time-step. The time-derivative $\dot{v}_x$ of the advected transverse velocity component v_x at cell interface $i+1/2$ is given by

$$\dot{v}_x=-\rho_x u_x\left(\frac{\partial v}{\partial\xi}\right), \tag{6}$$

where subscript x will, henceforth, denote a flow variable evaluated at the cell interface $i+1/2$ and the dot will denote the corresponding time-derivative. The analytic evaluation of cell-interface variables and their first time derivatives is the main outcome of the GRP analysis, and we refer to Reference 4 for details. Here we shall assume that these values have already been evaluated for all primitive variables, i.e. for u, v, ρ, p, and we proceed to specify the ensuing expressions for flux components and their time-derivatives. The flux components are given by

$$\mathbf{F}(\mathbf{U})_{i+1/2}^{n}=\begin{bmatrix}\rho_x u_x\\ \rho_x u_x^2+p_x\\ \rho_x u_x v_x\\ u_x\left[\dfrac{\gamma}{\gamma-1}p_x+\dfrac{1}{2}\rho_x(u_x^2+v_x^2)\right]\end{bmatrix}. \tag{7}$$

By taking the time-derivative of the flux components given in equation (7), the following expression is obtained:

$$\left[\frac{\partial}{\partial t}\mathbf{F}(\mathbf{U})\right]_{i+1/2}^{n}=\begin{bmatrix}\rho_x\dot{u}_x+\dot{\rho}_x u_x\\ 2\rho_x u_x\dot{u}_x+\dot{\rho}_x u_x^2+\dot{p}_x\\ \rho_x u_x\dot{v}_x+\rho_x\dot{u}_x v_x+\dot{\rho}_x u_x v_x\\ \dot{u}_x\left[\dfrac{\gamma}{\gamma-1}p_x+\dfrac{1}{2}\rho_x(u_x^2+v_x^2)\right]+u_x\left[\dfrac{\gamma}{\gamma-1}\dot{p}_x+\dfrac{1}{2}\dot{\rho}_x(u_x^2+v_x^2)+\rho_x(u_x\dot{u}_x+v_x\dot{v}_x)\right]\end{bmatrix}, \tag{8}$$

where the time-derivative of v_x is given by equation (6) and all other variables along with their time-derivatives are evaluated from the analytic expressions resulting from the GRP analysis (for details see Reference 4).

The only remaining feature of the 2D scheme is the Boundary Conditions (BC). The BC at rigid walls are a zero value of the normal velocity component. In the numerical scheme, this BC implies zero value for all flux components at cell boundaries that lie along a rigid wall, except for the pressure part of the momentum flux. Thus, the wall pressure constitutes the corresponding momentum flux. At walls of constant x or constant y the implementation of this BC (in accordance with the GRP scheme) is performed by solving a rigid-wall GRP at each x-facing or y-facing cell interface.

At an oblique wall (Figure 5), we resort to the following split BC scheme. In each direction (x or y), the segment of an oblique wall within a cell is replaced by a step having an x-facing

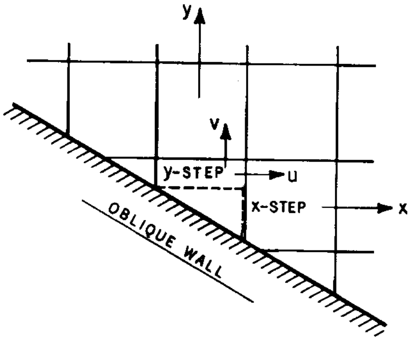

Figure 5. Oblique-wall boundary scheme. The wall segment within each cell is split into a *x*-step and a *y*-step

segment and a *y*-facing segment. During the performance of L_x^1, a GRP is solved at the *x*-facing step taken as a rigid wall, and likewise during the L_y^1 phase. The respective wall pressures and their first time-derivatives are then used in the expression for the momentum flux. As for the geometrical aspects of integrating the conservation laws according to equation (2) at the partial cells formed by an oblique wall (Figure 5), they are accounted for as follows. First, all fluxes are multiplied by the actual length of the respective cell-interface segment. Second, the actual cell volume is evaluated and is used to replace Δx in the conservation laws given by equation (2). We note that since the full volume of a regular cell is $\Delta x\ \Delta y$, this scheme reverts to equation (2) in the case of a regular cell.

In the present study, we also employed an inflow BC for the grid boundary through which the incident shock entered the test section. Assuming a negligible attenuation rate of the incident shock, we simply specified the inflow BC as the constant values corresponding to the flow behind the incident shock, according to the Rankine–Hugoniot relations, based on the measured shock wave Mach number and the initial air pressure and temperature prior to the shot. This BC is valid as long as no reflected waves reach the corresponding grid boundary.

RESULTS AND DISCUSSION

The initial conditions of the various experiments which will be discussed in the following are summarized in Table I. The experiments cover two different incident shock wave Mach numbers, $M_i \approx 1{\cdot}26$ and $M_i \approx 1{\cdot}48$ for the same reflecting wedge angle $\theta_w = 55°$, and two different reflecting wedge angles $\theta_w = 55°$ and $\theta_w = 65°$ for the same incident shock wave Mach number, $M_i \approx 1{\cdot}26$. Consequently, the dependence of the phenomenon both on the incident shock wave Mach number and the reflecting wedge angle could be evaluated.

Holographic interferograms and numerical simulations were produced for each one of the three cases listed in Table I. The numerical simulations are presented in the following as constant density contours (i.e. isopycnics) having a density spacing designed to match the experimental holographic interferograms.

The density difference corresponding to one fringe shift in the holographic interferograms shown earlier is determined by the experimental set-up and can easily be calculated from

$$\Delta\rho = \frac{\lambda}{KL}, \tag{9}$$

where λ is the wave length of the light source by which the holographic interferogram was recorded (a ruby laser for which $\lambda = 694{\cdot}3$ nm in the present study), K is the Gladstone–Dale constant of the investigated gas (approximately $0{\cdot}225\ \mathrm{cm}^3\,\mathrm{g}^{-1}$ for dry air) and L is the width of the test section (60 mm in the presently used shock tube). Therefore, the density difference between two neighbouring fringes (i.e. isopycnics) in the holographic interferograms is $\Delta\rho = 5{\cdot}14 \times 10^{-5}\ \mathrm{g\,cm}^{-3}$.

Note that owing to a small air gap between the shock-tube end-wall and its upper wall, which can be clearly seen in all the holographic interferograms, the high pressure air behind the head-on reflected shock wave leaked through the gap. As a result, an expansion wave was generated at the upper edge of the shock-tube end-wall. This expansion wave, which can be clearly seen at its early stages in the upper-right corner of the holographic interferograms shown in Figures 6(c), 7(d) and 8(a), and which interacted later on with the investigated wave configuration as can be seen in the holographic interferograms shown in Figures 7(j) and 8(c), was not simulated in the numerical computations.

Three holographic interferograms were recorded for Case 1 of Table I. The first, Figure 6(a), for which $M_i = 1{\cdot}260$, shows a regular reflection prior to its head-on collision with the shock-tube end-wall, the second, Figure 6(c) for which $M_i = 1{\cdot}256$, and the third, Figure 6(e), for which $M_i = 1{\cdot}263$, show, respectively, the wave configurations at a short time and at a longer time after the regular reflection [shown in Figure 6(a)] reflected head-on from the shock-tube end-wall. Each holographic interferogram is accompanied by a corresponding numerical simulation [Figures 6(b), 6(d) and 6(f), respectively] which were obtained using a coarse mesh of 220 × 190 cells (all grids in this study had square cells) by the presently developed computer code. Note that unlike the single shot holographic interferograms which slightly differ from each other in their incident shock wave Mach numbers, the incident shock wave Mach numbers in the respective numerical simulations shown in Figures 6(b), 6(d) and 6(f) are identical, i.e. $M_i = 1{\cdot}263$.

Four holographic interferograms were recorded for Case 2 of Table I. The first, Figure 7(a), for which $M_i = 1{\cdot}477$, shows a regular reflection prior to its head-on collision with the shock-tube end-wall, the second, Figure 7(d), for which $M_i = 1{\cdot}488$, the third, Figure 7(g), for which $M_i = 1{\cdot}488$, and the fourth, Figure 7(j), for which $M_i = 1{\cdot}491$, show, respectively, the wave configurations at a short time, at a longer time and at an even longer time after the regular reflection [shown in Figure 7(a)] reflected head-on from the shock-tube end-wall.

Each holographic interferogram is accompanied by two corresponding numerical simulations [Figures 7(b), 7(c), 7(e), 7(f), 7(h), 7(i), 7(k) and 7(l), respectively]. The first of each pair of these corresponding numerical simulations, i.e. Figures 7(b), 7(e), 7(h) and 7(k), were obtained using a coarse mesh of 235 × 175 cells, and the second of each pair of these corresponding numerical simulations, i.e. Figures 7(c), 7(f), 7(i) and 7(l), were obtained using a fine mesh of 705 × 525 cells. As can be seen the ratio between the fine and the coarse meshes is 3:1 in each direction. A comparison of the fine and coarse mesh simulations clearly indicates a high degree of numerical convergence of the finer computations.

In order to illustrate the discontinuities (mainly the two sliplines, s_1 and s_2, emanating from the two triple points, T_1 and T_2, in Figure 2) better, the fine mesh computations were replotted using a value of $\Delta\rho$ six times smaller than that used in Figures 7(i) and 7(l). The results are shown in Figures 7(m) and 7(n), respectively. It should be noted again that while the holographic interferograms were obtained with incident shock wave Mach numbers in the range $1{\cdot}477 \leq M_i \leq 1{\cdot}491$, all the numerical simulations were obtained with an identical value of $M_i = 1{\cdot}488$.

Two holographic interferograms were recorded for Case 3 of Table I. The first, Figure 8(a), for which $M_i = 1{\cdot}251$, and the second Figure 8(c), for which $M_i = 1{\cdot}265$, show, respectively, the wave

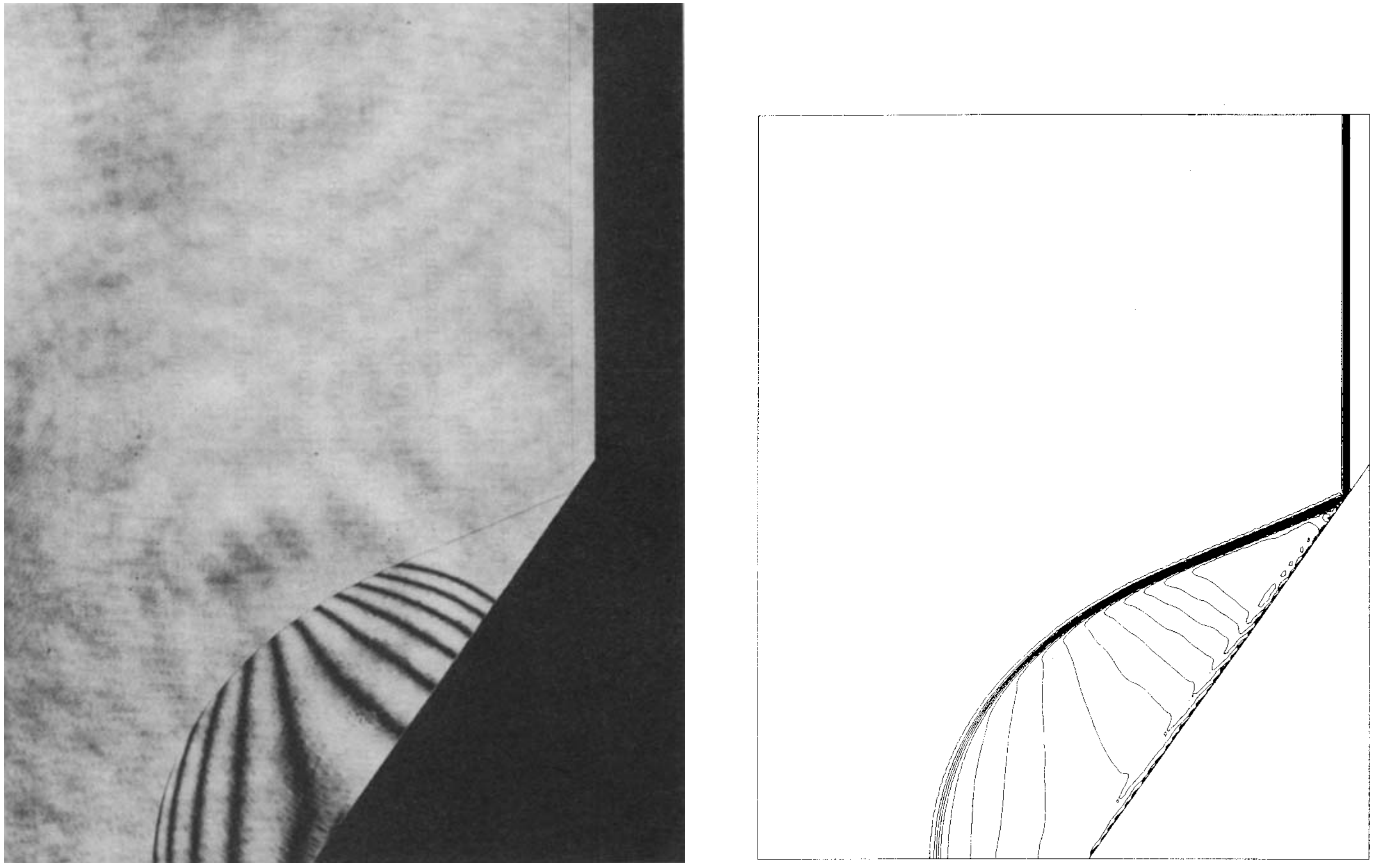

(a) (b)

Figure 6. (a) Holographic interferogram of a regular reflection prior to its head-on interaction with the end-wall. $M_i = 1{\cdot}26$, $\theta_w = 55°$. (b) Numerical simulation of the regular reflection shown in Figure 6(a). $M_i = 1{\cdot}263$, $\theta_w = 55°$.

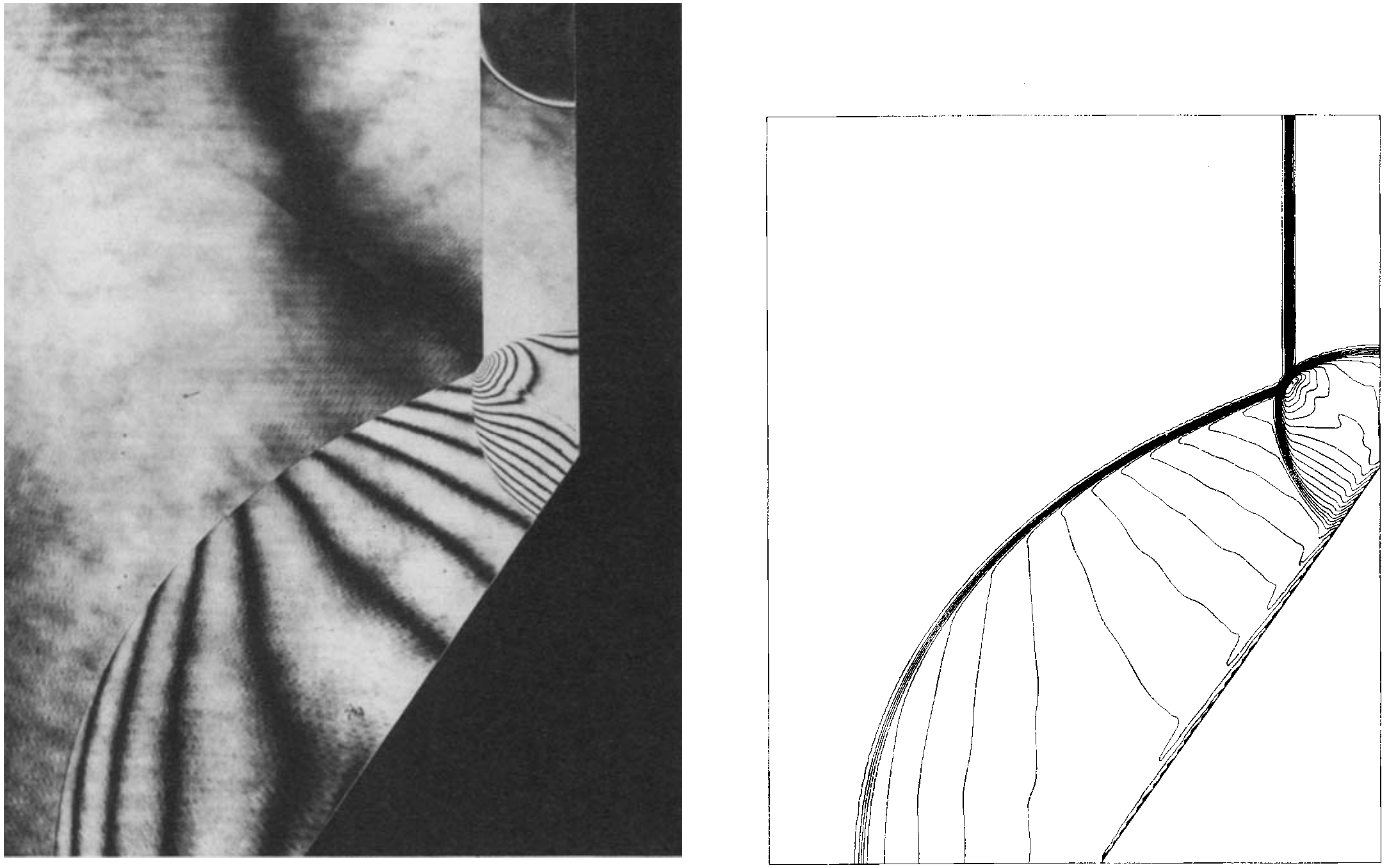

(c) (d)

Figure 6. (c) Hollographic interferogram of the wave configuration shortly after the regular reflection of Figure 6(a) collided head-on with the end-wall. $M_i = 1{\cdot}256$, $\theta_w = 55°$. (d) Numerical simulation of the wave configuration shown in Figure 6(c). $M_i = 1{\cdot}263$, $\theta_w = 55°$.

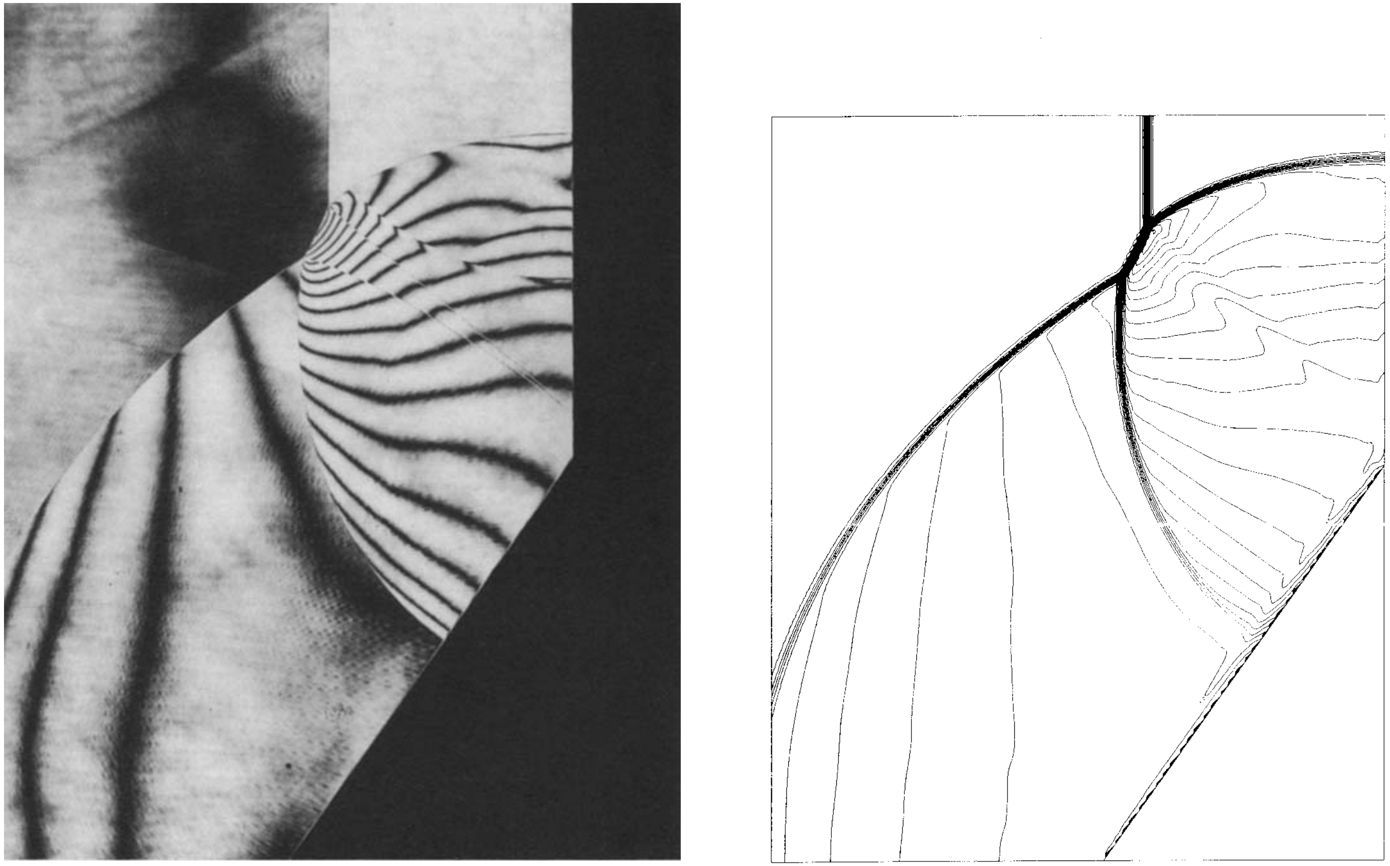

(e) (f)

Figure 6. (e) Hollographic interferogram of the wave configuration at a longer time after the head-on collision of the regular reflection with the end-wall. $M_i = 1{\cdot}263$, $\theta_w = 55°$. (f) Numerical simulation of the wave configuration shown in Figure 6(e). $M_i = 1{\cdot}263$, $\theta_w = 55°$

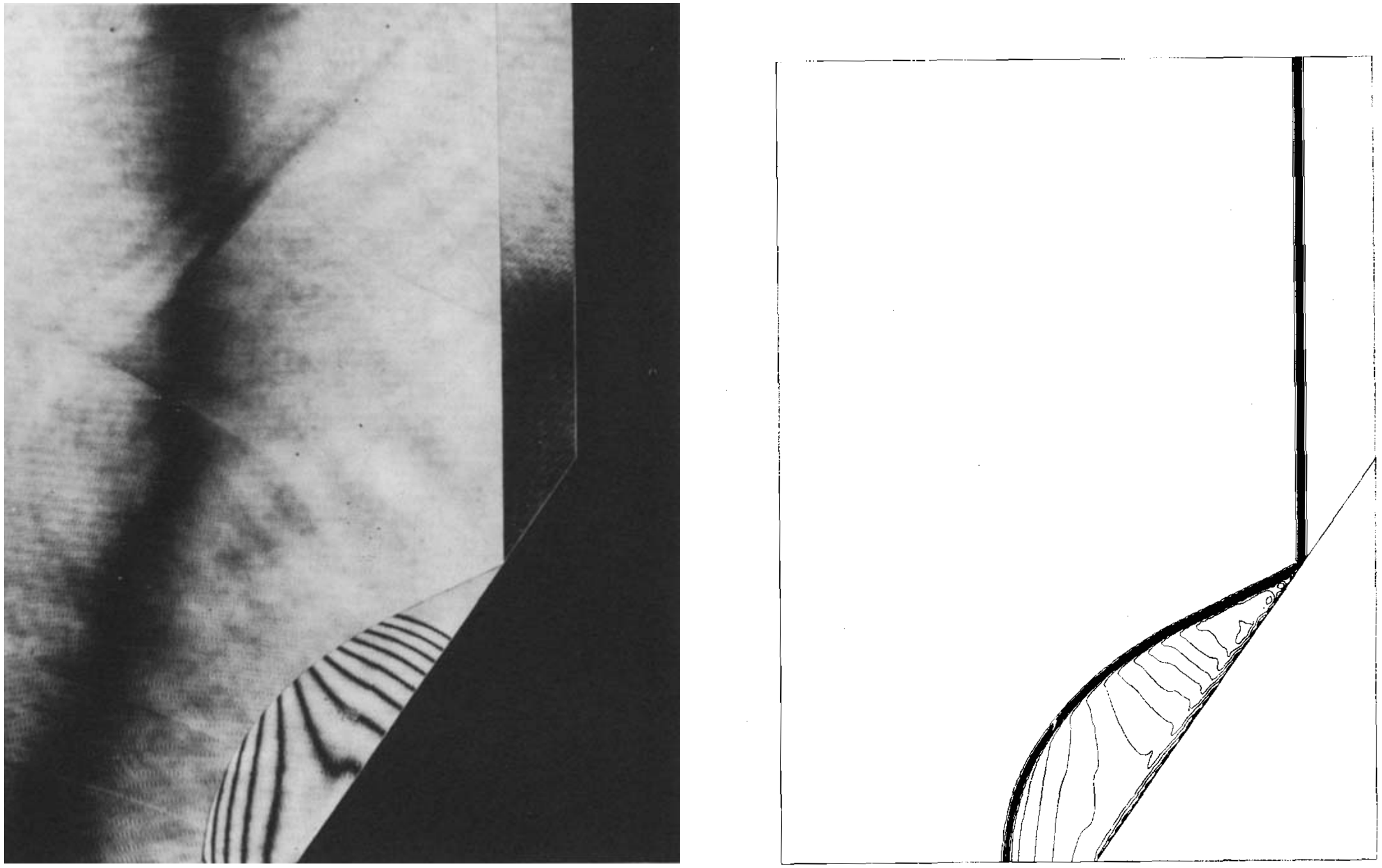

(a) (b)

Figure 7. (a) Hollographic interferogram of a regular reflection prior to its head-on interaction with the end-wall. $M_i = 1{\cdot}477$, $\theta_w = 55°$. (b) Numerical simulation, as obtained using a coarse mesh of 235 × 175 cells, of the regular reflection shown in Figure 7(a), $M_i = 1{\cdot}488$, $\theta_w = 55°$.

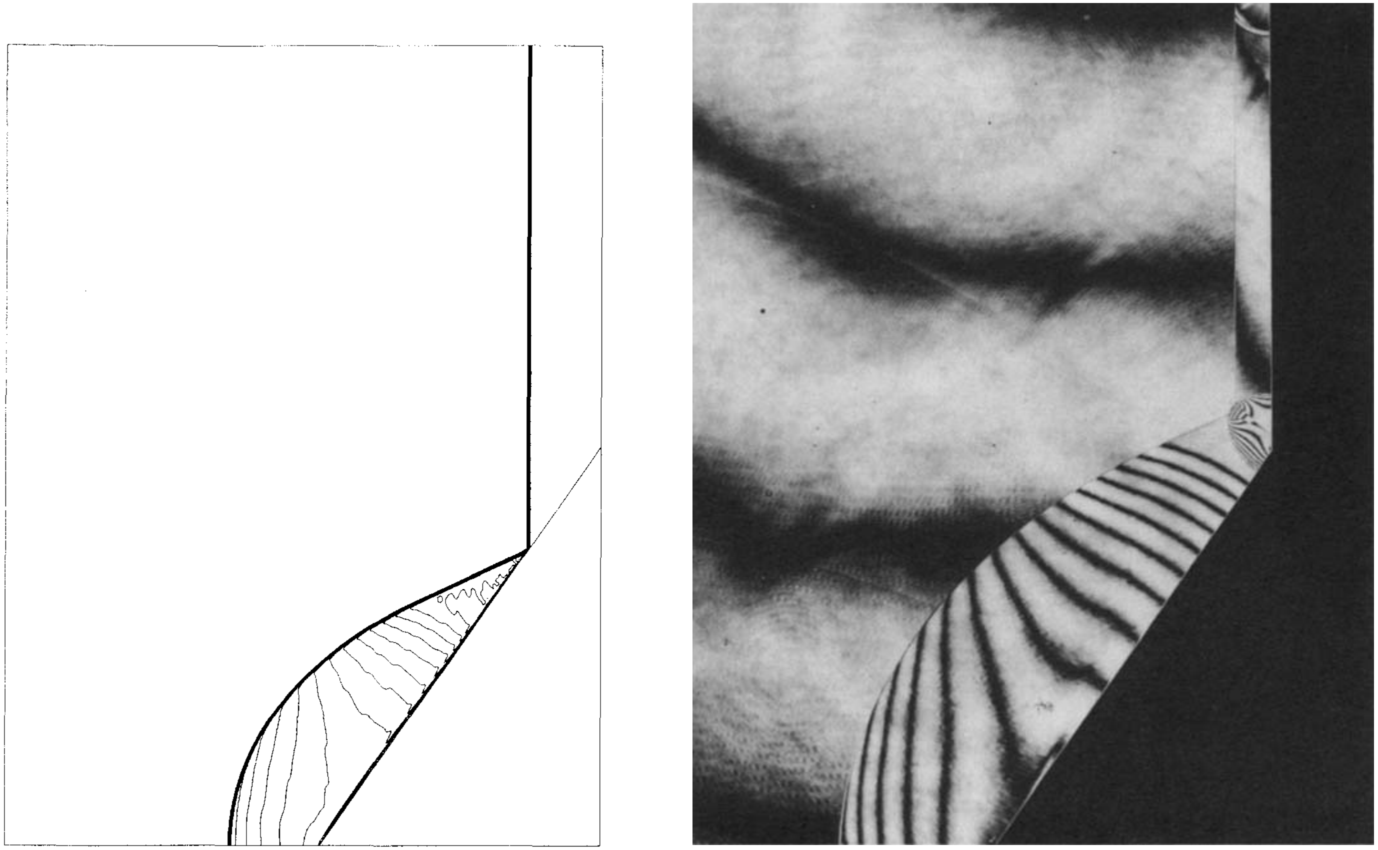

(c) (d)

Figure 7. (c) Numerical simulation, as obtained using a fine mesh of 705 × 525 cells, of the regular reflection shown in Figure 7(a). $M_i = 1{\cdot}488$, $\theta_w = 55°$. (d) Hollographic interferogram of the wave configuration shortly after the regular reflection of Figure 7(a) collided head-on with the end-wall. $M_i = 1{\cdot}488$, $\theta_w = 55°$.

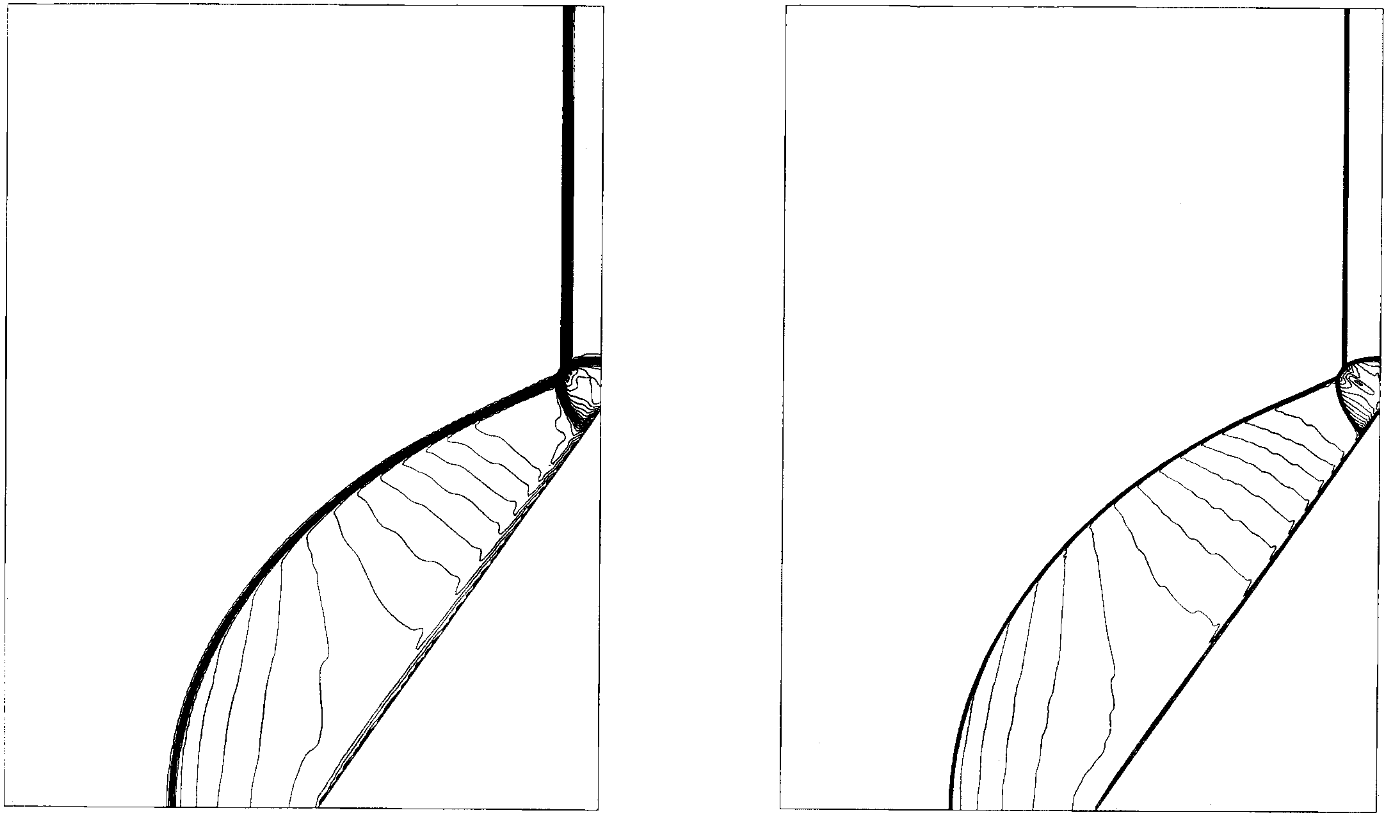

(e) (f)

Figure 7. (e) Numerical simulation, as obtained using a coarse mesh of 235 × 175 cells, of the wave configuration shown in Figure 7(d). $M_i = 1{\cdot}488$, $\theta_w = 55°$. (f) Numerical simulation, as obtained using a fine mesh of 705 × 525 cells, of the wave configuration shown in Figure 7(d). $M_i = 1{\cdot}488$, $\theta_w = 55°$.

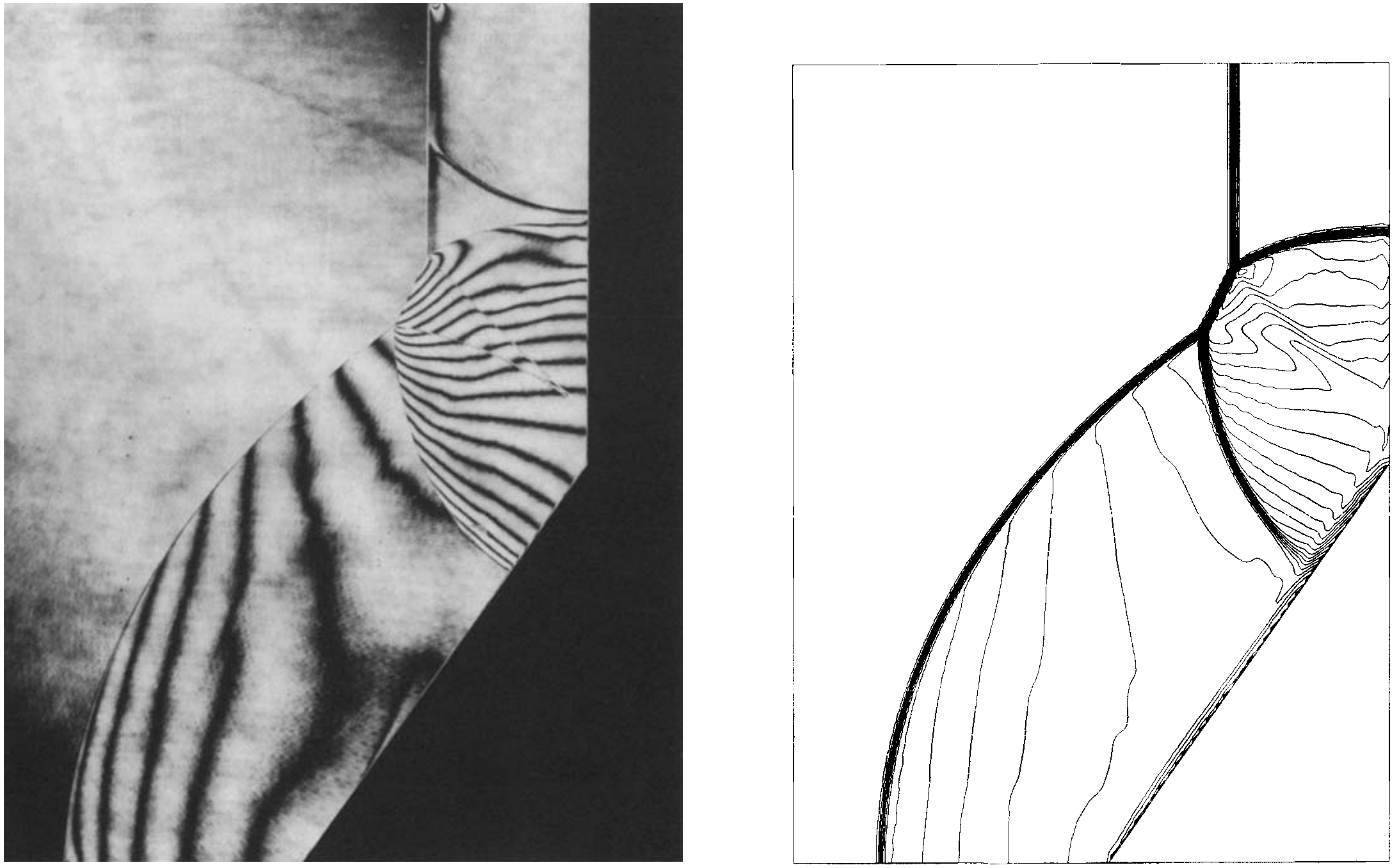

(g) (h)

Figure 7. (g) Hollographic interferogram of the wave configuration at a longer time after the head-on collision of the regular reflection with the end-wall. $M_i = 1{\cdot}488$, $\theta_w = 55°$. (h) Numerical simulation, as obtained using a coarse mesh of 235 × 175 cells, of the wave configuration shown in Figure 7(g). $M_i = 1{\cdot}488$, $\theta_w = 55°$.

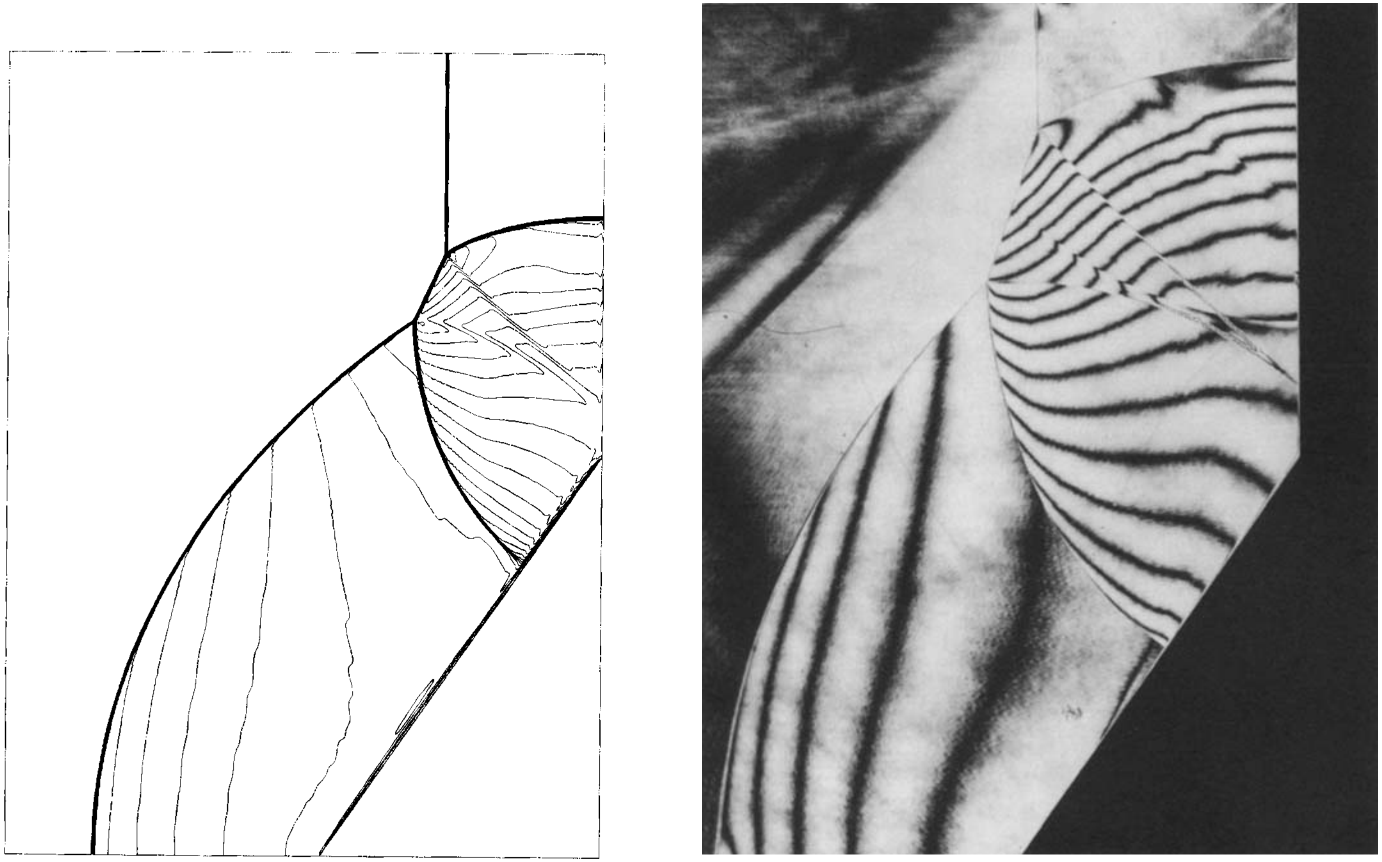

(i) (j)

Figure 7. (i) Numerical simulation, as obtained using a fine mesh of 705 × 525 cells, of the wave configuration shown in Figure 7(g). $M_i = 1{\cdot}488$, $\theta_w = 55°$. (j) Hollographic interferogram of the wave configuration at an even longer time after the head-on collision of the regular reflection of Figure 7(a) with the end-wall. $M_i = 1{\cdot}491$, $\theta_w = 55°$.

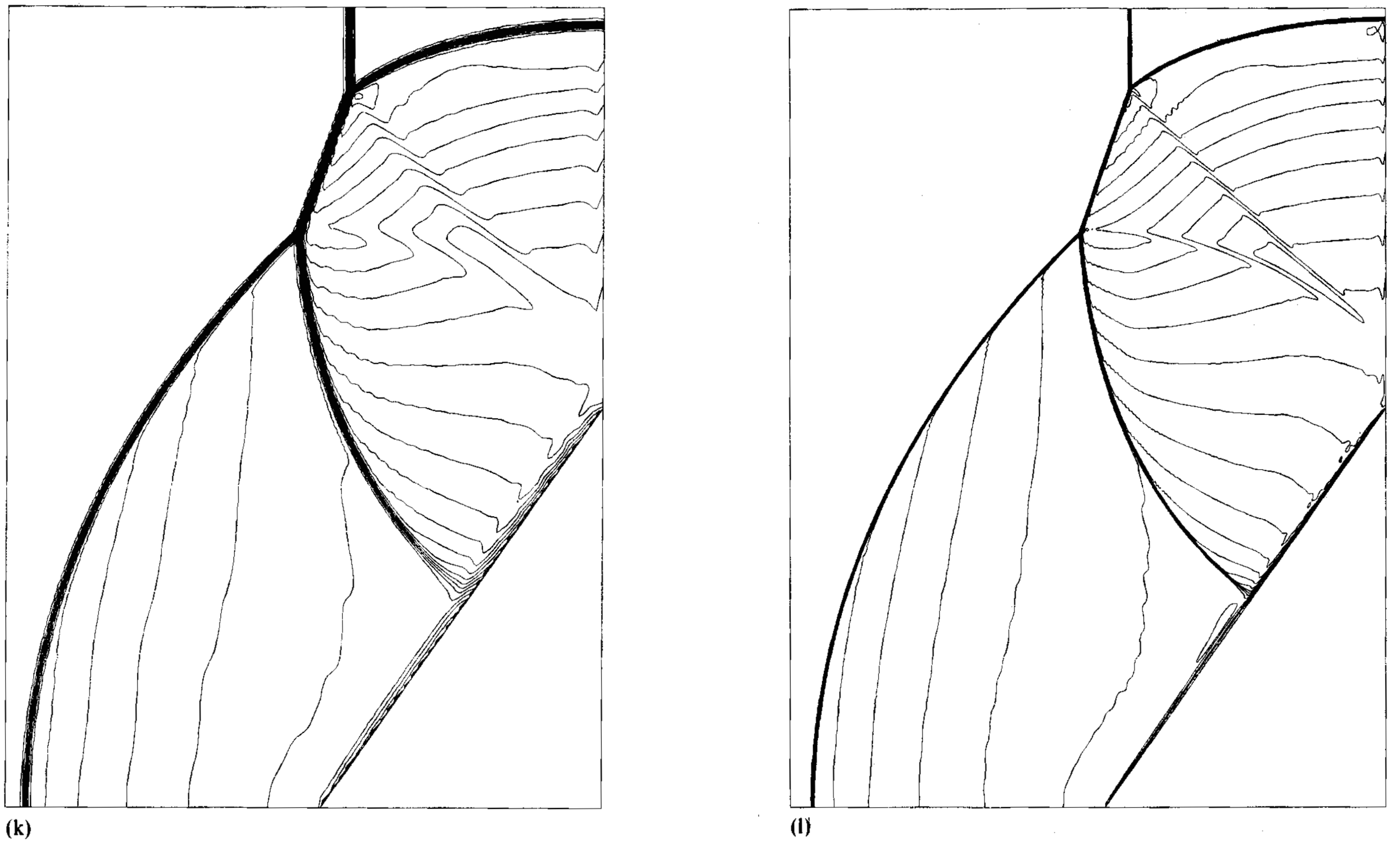

Figure 7. (k) Numerical simulation, as obtained using a coarse mesh of 235 × 175 cells, of the wave configuration shown in Figure 7(j). $M_i = 1{\cdot}488$, $\theta_w = 55°$. (l) Numerical simulation, as obtained using a fine mesh of 705 × 525 cells, of the wave configuration shown in Figure 7(j). $M_i = 1{\cdot}488$, $\theta_w = 55°$.

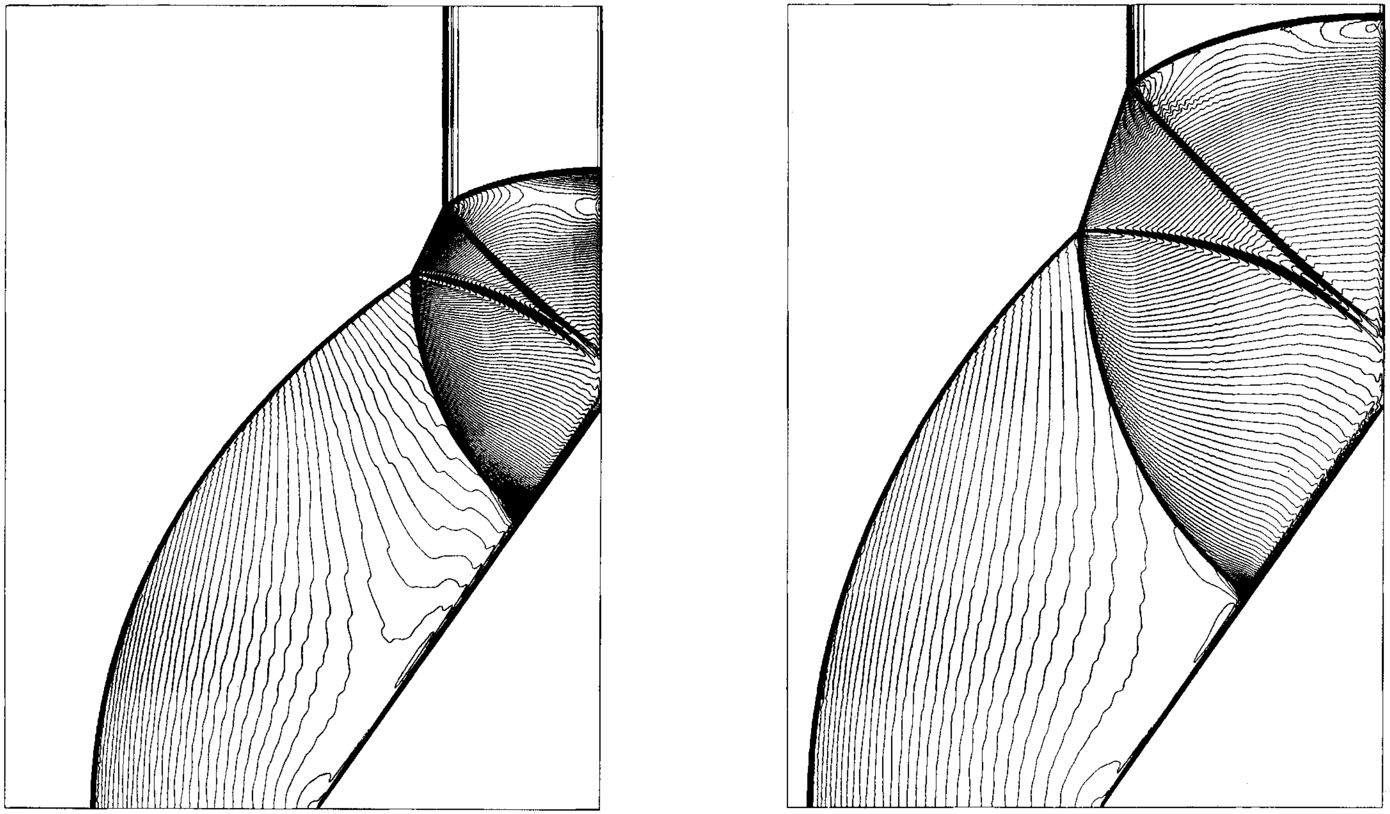

(m) (n)

Figure 7. (m) A replot of the fine mesh simulation shown in Figure 7(i) with a value of $\Delta\rho$ six times smaller. (n) A replot of the fine mesh simulation shown in Figure 7(l) with a value of $\Delta\rho$ six times smaller

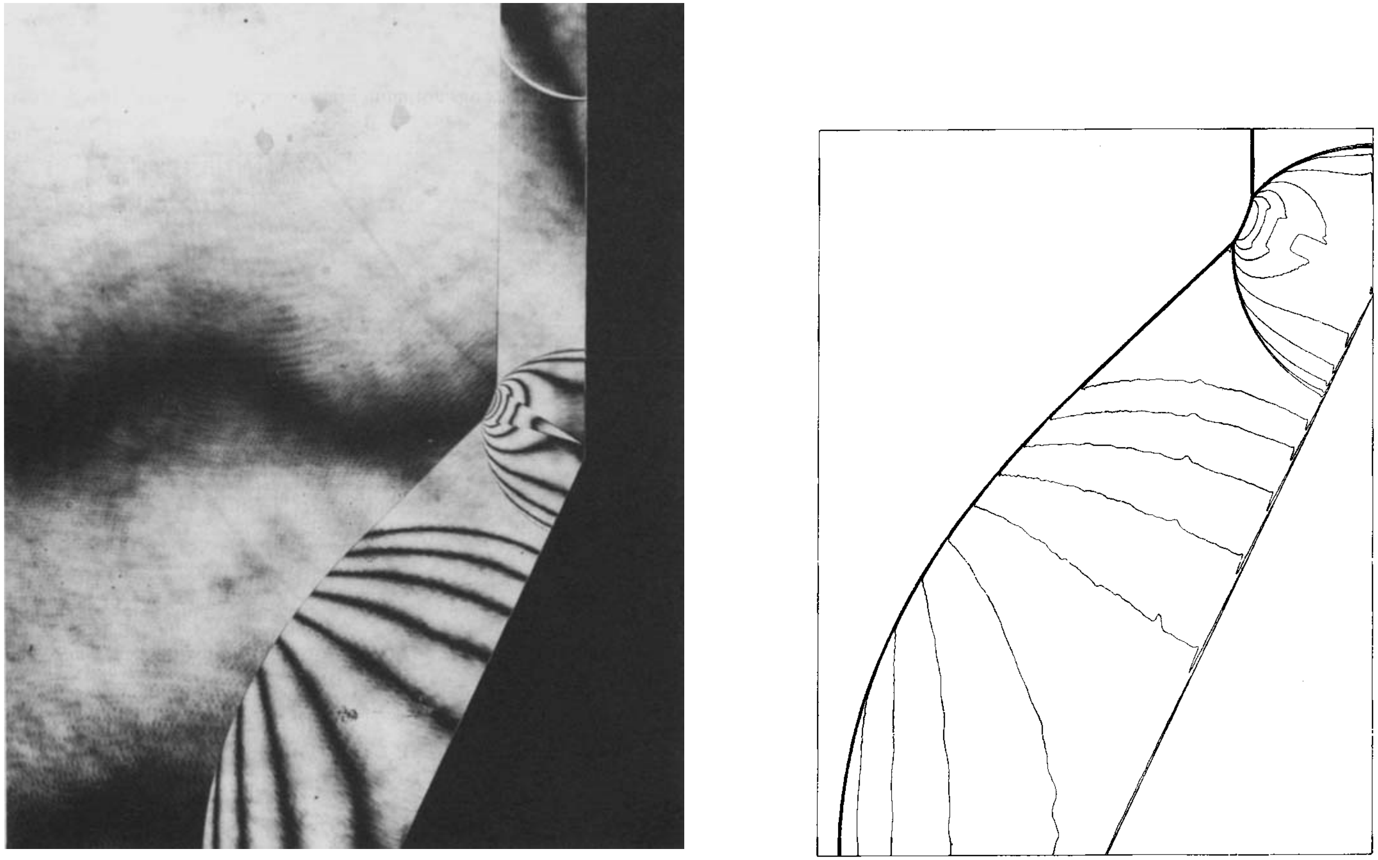

(a) (b)

Figure 8. (a) Hollographic interferogram of the wave configuration shortly after the regular reflection collided head-on with the end-wall. $M_i = 1{\cdot}251$, $\theta_w = 65°$. (b) Numerical simulation of the wave configuration shown in Figure 8(a). $M_i = 1{\cdot}251$, $\theta_w = 65°$.

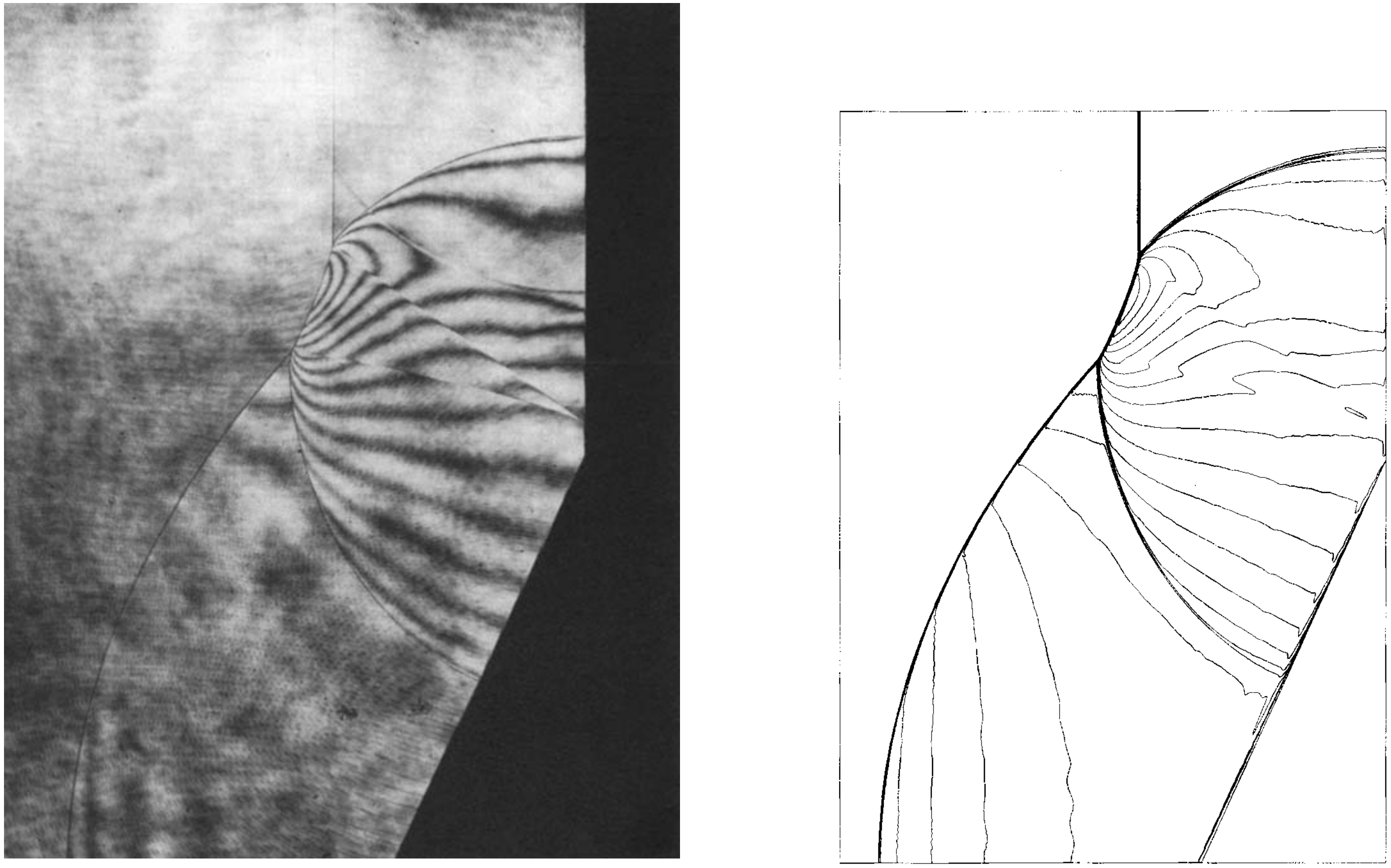

(c) (d)

Figure 8. (c) Hollographic interferogram of the wave configuration at a longer time after the head-on collision of the regular reflection with the end-wall. $M_i = 1{\cdot}265$, $\theta_w = 65°$. (d) Numerical simulation, as obtained using a fine mesh of 660 × 480 cells, of the wave configuration shown in Figure 8(c).

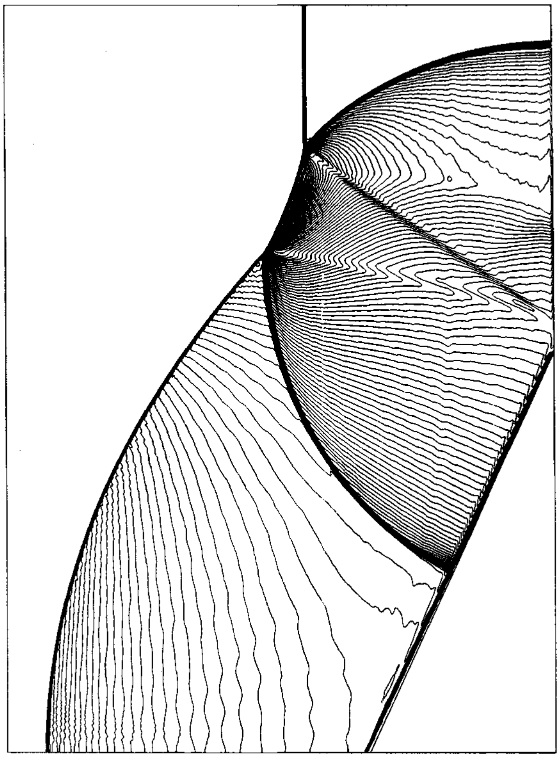

(e)

Figure 8. (e) A replot of the fine mesh simulation shown in Figure 8(d) with a value of $\Delta\rho$ six times smaller

configurations at a short time and at a longer time after the regular reflection reflected head-on from the shock-tube end-wall.

Each of these two holographic interferograms is accompanied by a corresponding numerical simulation [Figures 8(b) and 8(d), respectively] which were obtained using a fine mesh of 660 × 480 cells. Similar to the results shown in Figures 7(m) and 7(n) with the finer value of $\Delta\rho$, the computational results simulating the wave configuration shown in Figure 8(c) were replotted using a value of $\Delta\rho$ six times smaller than that used to draw Figure 8(d). The results, shown in Figure 8(e), clearly indicate that by applying this procedure, the two sliplines emanating from the two triple points become much more pronounced.

A comparison of the numerical simulations with the corresponding holographic interferograms clearly indicates that the presently developed computer code is capable of excellently reproducing both the wave configurations at the various stages of the reflection process and the general shapes of the isopycnics.

The agreement is nearly perfect at the RR region as can be seen by comparing Figures 6(a) and 6(b), and Figures 7(a) and 7(b). The distortion of the numerical isopycnics at the oblique wall, which can be seen in Figures 6(b) and 7(b), is evidence of an imperfect implementation of the boundary condition along the oblique wall, which causes a numerical 'adjustment layer' of several cells near the wall. The agreement between the experimental results and the numerical simulations after the RR reflected head-on at the shock-tube end-wall is also nearly perfect. [cf. Figures 6(c) and 6(d), Figures 6(e) and 6(f), Figure 7(d) with Figure 7(e) or Figure 7(f), Figure 7(g) with

Figure 7(h) or Figure 7(i), and Figure 7(j) with Figure 7(k) or Figure 7(l).] At the corner region (the vicinity of point C in Figure 1), quite understandably the agreement is good but not perfect. It should be noted here that as shown by Ben-Dor and Glass,[7] a reproduction of the wave configuration does not guarantee a reproduction of the flow field properties, e.g. isopycnics, Consequently, the very good agreement between the experimental holographic interferograms and the corresponding numerical simulation constitutes a validation of the computational method, including the oblique-wall boundary condition.

It should also be mentioned that while the shock waves were clearly reproduced even by the coarse-mesh computations [see Figure 6(f)], a clear reproduction of the sliplines required a three-times-finer grid. [Compare Figures 7(h) and 7(i), and 7(k) and 7(l).] In addition, while with the coarse-mesh calculations the shock waves appear to be too thick, in the fine-mesh calculations they are almost as thin as in the holographic interferograms. [Compare Figures 7(b) and 7(c), Figures 7(e) and 7(f), and Figures 7(h) and 7(i).] Furthermore, when a finer drawing was generated by using a six-times smaller value of $\Delta\rho$, the numerically computed sliplines became as sharp and as clear as the numerically computed shock waves [see, for example, Figures 7(m) and 7(n)].

CONCLUSIONS

A plane symmetric 2D numerical code based on the GRP method was developed in order to simulate the head-on reflection of a regular reflection from the shock-tube end-wall.

The predictions of the numerical code were compared with the results from actual shock tube experiments which were obtained using double-exposure holographic interferometry. The comparison revealed that the presently developed numerical code can very well simulate this complex wave reflection phenomenon. The overall very good agreement constitutes a validation of the GRP based computational method, including the oblique-wall boundary condition.

ACKNOWLEDGEMENTS

The authors would like to thank Mr. O. Onodera from the Shock Wave Research Center (SWRC) of the Institute of Fluid Science (IFS) of Tohoku University in Sendai Japan for conducting the experiments. The continuous support and encouragement of Prof. K. Takayama, the Head of the SWRC is gratefully acknowledged.

REFERENCES

1. G. Ben-Dor, *Shock Wave Reflection Phenomena*, Springer, Berlin, 1991.
2. G. Ben-Dor, J. M. Dewey and K. Takayama, 'The reflection of a planar shock wave over a double wedge', *J. Fluid Mech.*, **176**, 483–520 (1987).
3. K. Itoh, K. Takayama and G. Ben-Dor, 'Numerical simulation of the reflection of a planar shock wave over a double wedge', *Int. j. numer. methods fluids*, **13**, 1153–1170 (1991).
4. M. Ben-Artzi and J. Falcovitz, 'An upwind second-order scheme for compressible duct flows', *SIAM J. Sci. Statist. Comput.*, **7**, 744–768 (1986).
5. G. Strang, 'On the construction and comparison of difference schemes', *SIAM J. Numer. Anal.*, **5**, 506–517 (1968).
6. B. Van-Leer, 'Towards the ultimate conservative difference scheme V', *J. Comput. Phys.*, **32**, 101–136 (1979).
7. G. Ben-Dor and I. I. Glass, 'Nonstationary oblique shock wave reflections: actual isopycnics and numerical experiments', *AIAA J.*, **16**, 1146–1153 (1978).